Contents lists available at ScienceDirect

Transactions of Nonferrous Metals Society of China

36(2026) 451−469

www.tnmsc.cn

Effect of annealing treatment on microstructure, mechanical properties and biodegradable behaviors of high-performance wrought Zn−0.1Mg alloy

Huan LIU [a*], Li-feng YE [a,b], Jing-bo LI [a], Chao SUN [c], Yu-na WU [a], Jia JU [d], Hang TENG [e], Jing-hua JIANG [a,f], Jing BAI [c], Feng XUE [c]

[a] College of Materials Science and Engineering, Hohai University, Changzhou 213200, China;
[b] Power China Huadong Engineering Corporation Limited, Hangzhou 311122, China;
[c] Institute of Medical Devices (Suzhou), Southeast University, Suzhou 215163, China;
[d] Jiangsu Key Laboratory of Advanced Structural Materials and Application Technology, Nanjing Institute of Technology, Nanjing 211167, China;
[e] Baowu Magnesium Technology Co., Ltd., Nanjing 211200, China;
[f] Suqian Research Institute of Hohai University, Suqian 223800, China

Abstract: To investigate the aging mechanisms and elucidate the correlations between unstable microstructure and performance in biodegradable Zn alloys, the accelerated aging experiment was conducted on a high-performance wrought Zn−0.1Mg alloy by annealing at 200 °C for varying durations. The findings reveal that the tensile strength of the alloy rapidly and significantly declines with prolonged annealing time, decreasing from 383 MPa for the as-received alloy to 102 MPa for the alloy subjected to 1440 min of annealing. The primary factors contributing to this considerable reduction in strength are static recrystallization, grain coarsening, and dislocation annihilation. Initially, the ductility of the alloy shows fluctuations, ultimately experiencing a marked decrease after extended annealing. This decline is linked to the grain growth and heightened texture intensity, while the unusual increase in ductility observed between 30 and 120 min of annealing is likely due to the formation of twins. In addition, due to rapid grain growth and an increase in precipitates and twins, the corrosion resistance of the alloy in Hank's solution has worsened, with the corrosion rate rising from 0.037 to 0.069 mm/a following 300 min of annealing.

Keywords: Zn−0.1Mg alloy; annealing; microstructure evolution; mechanical properties; corrosion behavior

1 Introduction

Zinc (Zn) alloys are regarded as ideal biodegradable metallic materials due to their favorable biodegradability, good biocompatibility, and ease of manufacturing [1,2]. Over the past decade, advancements in biodegradable Zn alloys have led to the clinical application of several medical devices made from high-performance Zn alloys [3−6]. Nonetheless, various limitations of Zn alloys still hinder their broader use in health and medical sectors [7,8]. Firstly, pure Zn and/or standard Zn alloys often demonstrate inadequate mechanical properties that do not fulfill the requirements for applications in cardiovascular stents or bone repair devices [9,10]. Secondly, the mechanical properties of Zn alloys tend to be unstable at ambient temperature owing to their relatively low recrystallization temperatures [11]. Therefore, a better understanding of the strengthening−toughening and aging mechanisms in Zn alloys is essential to address these issues.

Corresponding author: *Huan LIU, Tel: +86-15951082775, E-mail: liuhuanseu@hhu.edu.cn
https://doi.org/10.1016/S1003-6326(25)66975-5
Received 7 May 2024; accepted 18 December 2024

Alloying and plastic deformation are widely employed techniques for enhancing the strength and ductility of Zn alloys. The elements primarily incorporated into Zn alloys include Li, Mg, Ca, Mn, Cu, Sr, Ag, and certain rare-earth (RE) elements [12−15]. These elements can enhance the mechanical properties of Zn alloys by forming substitutional solid solutions and various secondary phases [14,15]. For example, the Mg_2Zn_{11} and $LiZn_4$ phases effectively improve the strength. As a result, Zn−Mg and Zn−Li systems are two typical high-strength Zn alloys [16,17]. In contrast, the $MnZn_{13}$ and $CuZn_4$ phases are deformable during loading, which is beneficial to the ductility/plasticity of Zn alloys, even achieving superplasticity [18,19]. With respect to the plastic deformation, conventional processing, including extrusion and rolling, is commonly carried out. Most studies have demonstrated that the refinement of microstructures (including the grain size and secondary phase) significantly contributes to the strength and ductility of Zn alloys [17,20−22]. Additional factors, such as twinning and texture, also affect the mechanical properties; however, their influence is less significant compared to the grain size refinement in wrought Zn alloys [23−26]. Consequently, severe plastic deformation (SPD) methods are commonly utilized for producing high-performance Zn alloys, with equal channel angular pressing (ECAP) being particularly prominent [27−29]. Through this technique, recent research has effectively developed Zn−Mg, Zn−Cu, Zn−Cu−Mg, and Zn−Mg−Ag alloys exhibiting both high strength and high ductility [27,28,30].

The aging process of Zn alloys signifies that their mechanical properties, particularly ductility, are unstable due to microstructural changes occurring during natural storage at room temperature [8,31–33], which poses significant risks for biodegradable materials. Implants, such as stents or bone nails, must retain their mechanical characteristics and structural integrity for 90−180 d within the human body. However, the decline in mechanical properties due to aging at about 37 °C can lead to premature device failure, negatively impacting patients' health and quality of life [7]. The aging of Zn alloys is caused by their low melting point and limited thermal stability of the microstructures. This results in easy diffusion of solute atoms and grain boundaries, which affects grain morphology and phase precipitation, ultimately leading to a decrease in ductility [19,34]. Prior studies on the aging behavior of the ECAPed Zn−0.5Cu alloy through accelerated aging (such as annealing at 200 °C) demonstrated that grain coarsening and texture enhancement during annealing were chiefly responsible for the reductions in both strength and ductility [35].

Because Zn−Mg alloys are completely different from Zn−Cu alloys in terms of their mechanical characteristics, high-strength and biocompatible Zn−Mg alloys hold more potential in real applications. Thus, determining the aging behavior and mechanisms of Zn−Mg alloys and unpicking their impacts on the corresponding mechanical and biodegradable behaviors are important. YE et al [36] developed a low-alloyed, high-strength, ductile, and suitable biodegradable Zn−0.1Mg alloy with mechanical properties superior to those of previously developed low-alloying Zn−Mg alloys (≤1.0 wt.%) and comparable to those of the developed Mg- and Fe-based alloys [37]. Moreover, the biodegradability of Zn alloys is usually more suitable than that of Mg- and Fe-based alloys. However, Mg and Fe alloy systems usually do not experience aging issues due to their relatively high melting points compared to Zn alloys [38−40]. Therefore, understanding the aging behaviors and mechanisms of Zn alloys is of great significance.

Consequently, a high-performance, low-alloyed Zn−0.1Mg ECAPed alloy was utilized in this study, and an accelerated aging process was conducted to examine its microstructural evolution, mechanical properties, and biodegradation behaviors. By the characterization of microstructures and properties, the aging mechanisms of the developed Zn−Mg alloys and their corresponding effects on the properties were clarified.

2 Experimental

2.1 Materials and processing

A high-performance wrought Zn−0.1Mg (wt.%) ECAPed alloy was selected for this study. The detailed casting and processing methods have been described in Ref. [36]. Annealing treatment was conducted in a KSL−1200X chamber electric resistance furnace. The temperature was set at 200 °C. When the furnace temperature reached the target temperature, a small crucible with methyl

silicone oil was placed in the furnace and held for 10 min to ensure that the temperature stabilized at (200±1) °C. Afterward, the sample was immersed in methyl silicone oil to maintain uniform heating and avoid oxidation. Once the annealing period reached, the sample was removed immediately using tweezers and cooled in air. In this study, the annealing time was set at 0.25, 1, 5, 30, 120, 300, and 1440 min, respectively. According to the evolution of the mechanical properties, four representative samples with annealing time of 1, 5, 30, and 300 min were then chosen for microstructure characterization and evaluation of corrosion behavior.

2.2 Microstructure characterization and mechanical properties tests

The microstructures of the annealed Zn−0.1Mg alloys were characterized using an Olympus BX51M optical microscope (OM), a ZEISS Sigma 300 field emission scanning electron microscope (SEM) equipped with a GENESIS 60S energy dispersive X-ray spectrometer (EDS), an electron back-scattered diffraction technique (EBSD), and a Tecnai G2 transmission electron microscope (TEM). The metallographic and SEM samples were ground with SiC abrasive papers ($180^{\#}$−$2000^{\#}$), polished with 2.5 μm diamond spray, and chemically etched with a solution of 2 g CrO_3 + 0.15 g Na_2SO_4 + 10 mL H_2O chromic acid for 30 s. The TEM samples were polished into thin foils with a thickness of ~50 μm with $2000^{\#}$ SiC papers and then thinned via twin-jet electropolishing. For EBSD observation, the samples were mechanically polished, followed by electropolishing at 32 V for 300 s in 95 vol.% alcoholic + 5 vol.% perchloric acid solution at −40 °C. Channel 5 software was employed to analyze the measured EBSD data.

The tensile tests of the annealed samples were conducted using a CMT−5105 electronic universal testing machine at a constant strain rate of 1×10^{-3} s^{-1} and room temperature. The tensile samples exhibited a dumbbell-like shape with gauge dimensions of 6 mm × 2.5 mm × 2 mm. To ensure that the results were reproducible, three parallel samples were used for each annealing condition.

2.3 Corrosion behavior tests

The corrosion behavior of the annealed Zn−0.1Mg alloys was investigated using immersion and electrochemical tests in Hank's solution at (37±0.5) °C, with a pH of 7.40±0.1. In accordance with ASTM-G 31—72, the specific components of Hank's solution include: 8.00 g/L NaCl, 1.00 g/L glucose, 0.40 g/L KCl, 0.35 g/L $NaHCO_3$, 0.14 g/L $CaCl_2$, 0.06 g/L $MgSO_4\cdot7H_2O$, 0.10 g/L $MgCl_2\cdot6H_2O$, 0.06 g/L $Na_2HPO_4\cdot12H_2O$, and 0.06 g/L KH_2PO_4.

The electrochemical test was conducted using a standard three-electrode system with a CHI660C electrochemical workstation. The working electrode was represented by the test alloy with an exposed area of 10 mm × 10 mm, while the reference electrode was the saturated calomel electrode, and the auxiliary electrode was the platinum electrode. Prior to testing, the sample surface was mechanically polished using sandpapers, followed by diamond spray polishing, and subsequently cleaned and dried through ultrasonication in alcohol. An open circuit potential (OCP) test was carried out for 1 h to achieve stability at the OCP for the sample. The voltage for the potential dynamic polarization (PDP) curve was adjusted from −1.5 to −0.6 V, with a scanning speed of 0.1 mV/s. Electrochemical impedance spectroscopy (EIS) test was executed at an amplitude of ±10 mV within a scanning frequency range from 10^{-5} to 10^{-2} Hz. To ensure the reliability of the test results, all alloys underwent testing at least three times. Ultimately, ZsimDemo software was utilized to derive the fitted circuit corresponding to the electrochemical results.

Prior to the immersion tests, the samples (10 mm × 10 mm × 2 mm) were polished with SiC-paper graded from $180^{\#}$ to $2000^{\#}$ and then cleaned ultrasonically using anhydrous ethanol before drying. The samples were subsequently immersed in Hank's solution in a polyethylene centrifuge tube for a duration of 30 d. Each group included three parallel samples. During the entire immersion period, the centrifuge tube was maintained in a water bath at (37±0.5) °C. After immersion, the samples were rinsed with deionized water and dried for subsequent characterization. The surface corrosion products were removed using a solution of 200 g/L CrO_3 + 10 g/L $AgNO_3$ after examination. The morphology and composition of the surface were analyzed using SEM and EDS before and after immersion. Finally, the corrosion rate of the alloys was determined from the immersion tests in accordance with ASTM G31 using Eq. (1):

$$R_C=\frac{8.76\times10^4(m_0-m_1)}{S\cdot\rho\cdot t} \quad (1)$$

where R_C is the corrosion rate (mm/a), m_0 is the mass of the sample before immersion (g), m_1 is the mass of the sample after immersion and removal of the corrosion products (g), S is the area of the immersed surface (cm^2), ρ is the alloy density (g/cm^3), and t is the immersion time (h).

3 Results and discussion

3.1 Influence of annealing time on mechanical properties of wrought Zn−0.1Mg alloy

Figure 1(a) illustrates the engineering stress−strain curves of the ECAPed Zn−0.1Mg alloy following annealing for varying durations, while the corresponding strength and elongation values are presented in Fig. 1(b). The as-received alloy exhibits remarkable overall mechanical properties, with an ultimate tensile strength (UTS) of 383 MPa and an elongation (EL) of 45%, as detailed in a previous study [36]. After annealing, the strength shows a continuous decline with increasing annealing time. The elongation values fluctuate, initially decreasing during the short annealing period (within 5 min),

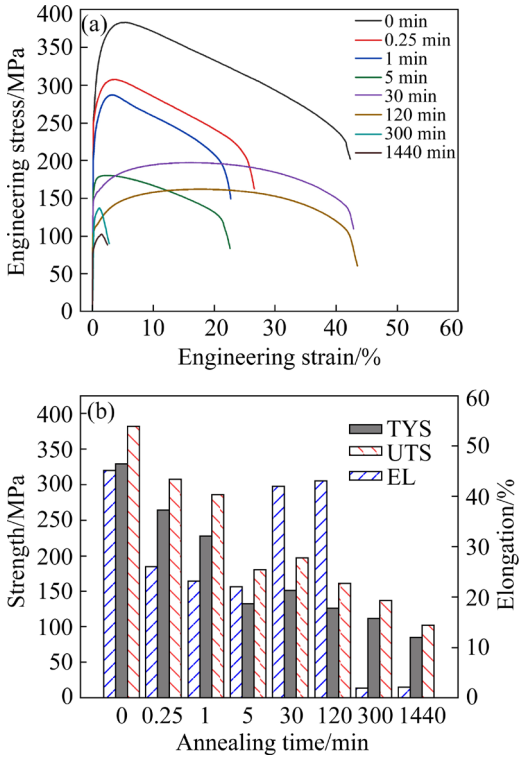

Fig. 1 Tensile properties of annealed Zn−0.1Mg alloys: (a) Engineering stress−strain curves; (b) Typical strength and elongation values

followed by an abnormal increase from 30 to 120 min, and then a rapid decline after 300 min. When the annealing duration exceeds 300 min, the mechanical properties significantly deteriorate, resulting in a UTS of about 100 MPa and an elongation of merely 2%. Overall, annealing at 200 °C negatively impacts the mechanical properties of the alloy.

3.2 Microstructure evolution of annealed alloys

On the basis of the tensile curves shown in Fig. 1(a), four alloys with representative annealing time, i.e., 1, 5, 30, and 300 min, were selected for the microstructure characterization. The optical microscopy (OM) images of the four annealed alloys are shown in Fig. 2. The grain size of the alloy increases gradually, and the grain boundaries become clear with increasing annealing time. Moreover, a small number of twins are found in the samples with longer annealing time. In addition, Fig. 3 shows SEM images of the Zn−0.1Mg alloys after four annealing treatments. Apart from the distinct grain growth, a broken eutectic structure is identified at the grain boundaries, which are still aligned along the pressing direction, suggesting that the eutectic structure is thermally stable during long-term annealing. In our previous research [36], the eutectic structures were demonstrated to be α-Zn, Mg_2Zn_{11}, and nanosized $MgZn_2$ phases.

Figure 4 shows the TEM images of the wrought Zn−0.1Mg alloys after annealing for different durations. The grains are equiaxed, and the broken eutectic structures are distributed at the grain boundaries. Moreover, as marked by the yellow and red arrows, precipitates within grains and at grain boundaries are observed in the four samples. The selected area electron diffraction (SAED) patterns of the precipitates are presented in the insets of Figs. 4(b) and (d), indicating that the precipitates within the grains and at the grain boundaries are both $MgZn_2$ phases. This occurrence is attributed to the significant deformation experienced by the alloy, resulting in a substantial amount of the stored deformation energy that enhances the tendency for precipitation, leading to the formation of the $MgZn_2$ phase during the annealing process [30]. Additionally, the grain size of the alloy increases with prolonged annealing time (Figs. 4(a, c, e, g)), and twins become observable after extended annealing periods (Fig. 4(h)), corroborating the findings from the metallographic and SEM analyses.

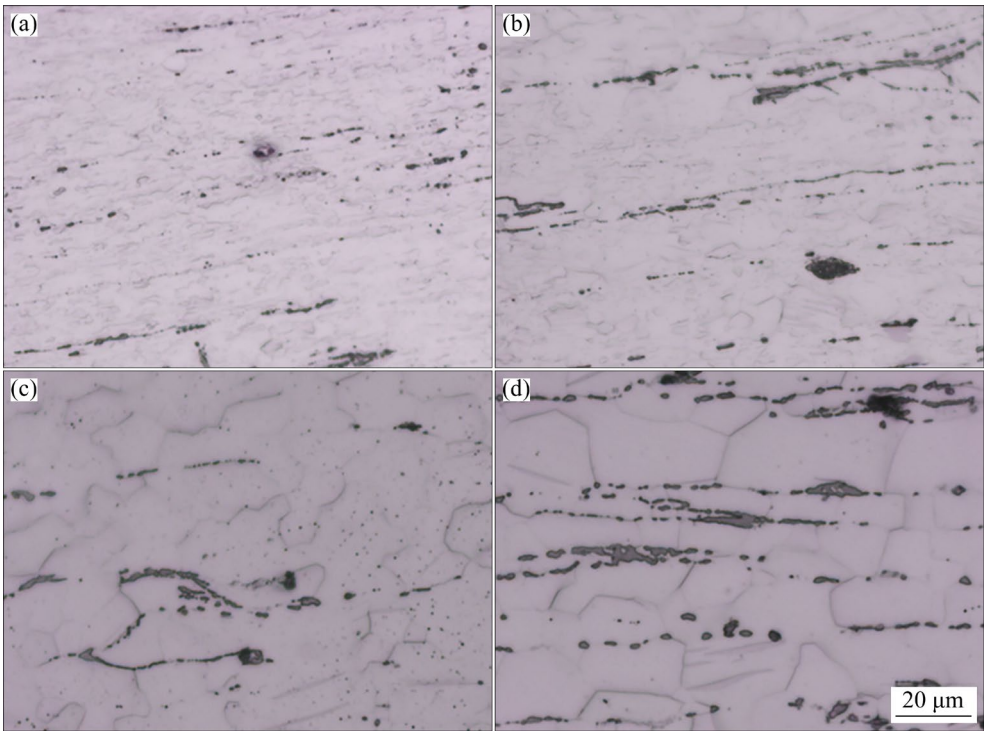

Fig. 2 OM images of four annealed Zn−0.1Mg alloys: (a) 1 min; (b) 5 min; (c) 30 min; (d) 300 min

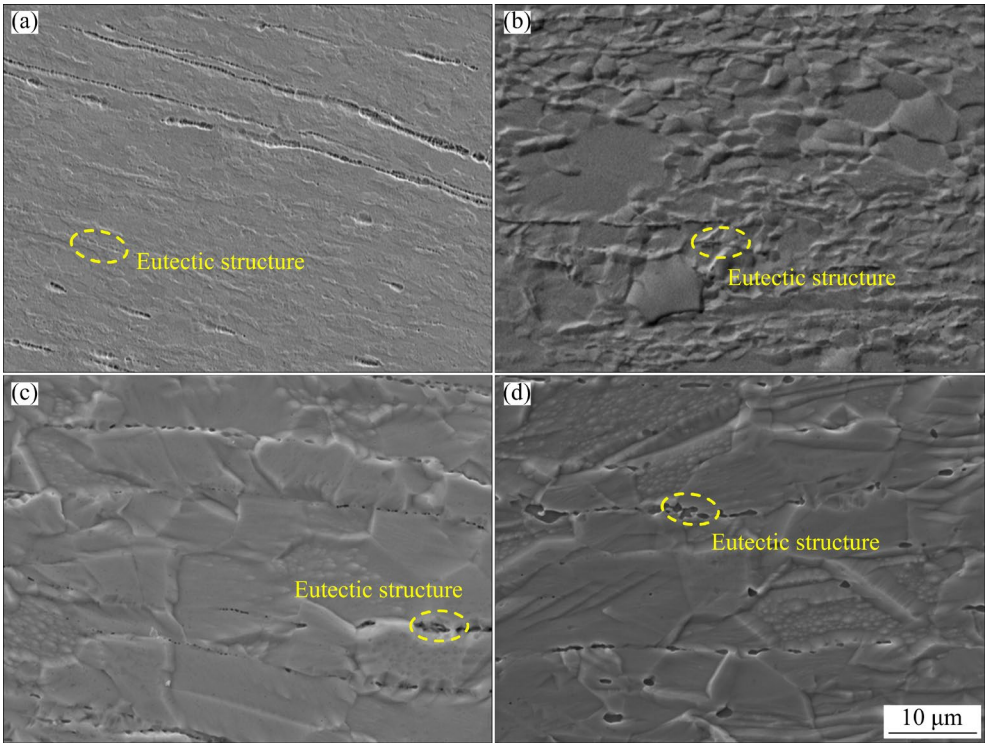

Fig. 3 SEM images of four annealed Zn−0.1Mg alloys: (a) 1 min; (b) 5 min; (c) 30 min; (d) 300 min

The inverse pole figures (IPFs) and the related grain size distribution diagrams for the four annealed alloys are illustrated in Fig. 5. A uniform microstructure is identified in the sample, which exhibits a large number of equiaxed grains after 1 min of annealing. After an annealing period of 5 min, the microstructure shows slight irregularities, with grain size increasing from 1.40 to 2.20 μm. With longer annealing time, the grain distribution becomes progressively nonuniform, resulting in an average

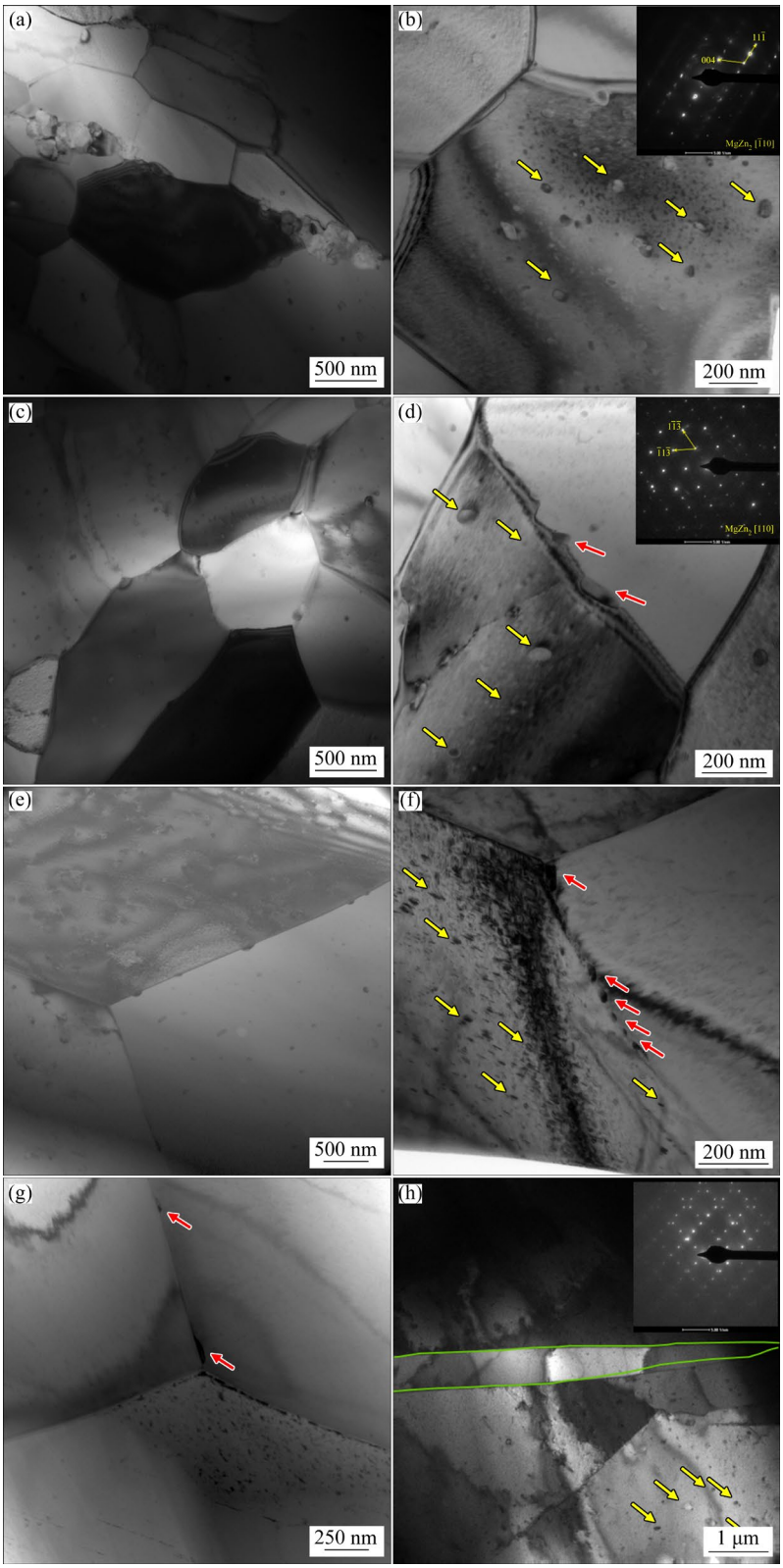

Fig. 4 TEM images of four annealed Zn−0.1Mg alloys: (a, b) 1 min; (c, d) 5 min; (e, f) 30 min; (g, h) 300 min

grain size of 17.80 μm after 300 min. It is clear that the grain growth rate decreases as annealing time extends, aligning with findings related to Zn−Cu alloys [35]. In the initial annealing stage (1−30 min), the stored deformation energy from ECAP is sufficient to facilitate the grain growth, leading to a high rate of grain boundary migration that accelerates this process. However, as the annealing

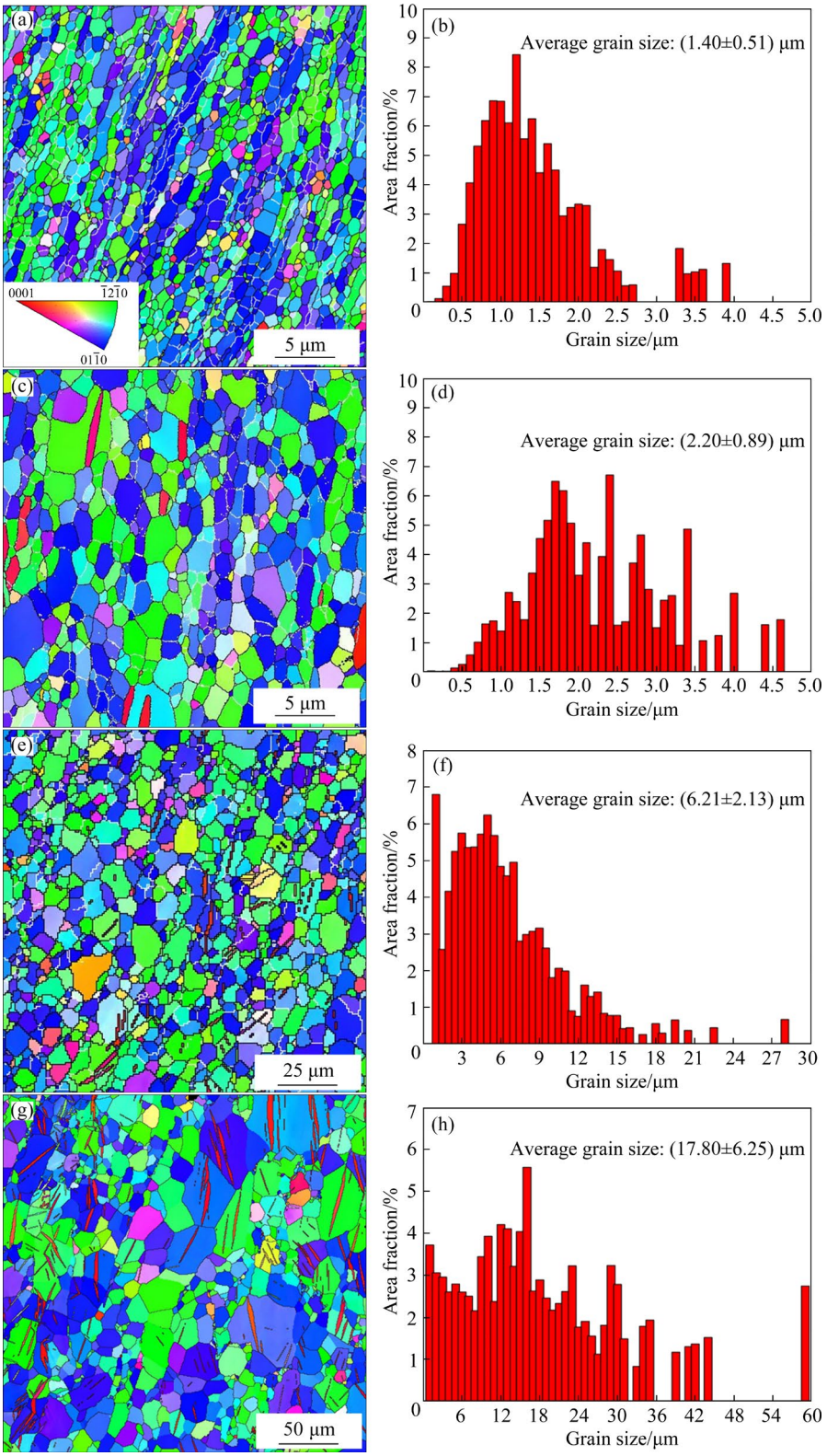

Fig. 5 IPFs and grain size distributions of four annealed Zn−0.1Mg alloys: (a, b) 1 min; (c, d) 5 min; (e, f) 30 min; (g, h) 300 min

duration increases to 300 min, a considerable amount of stored deformation energy is depleted by the grain growth, which reduces the grain boundary mobility [41−44]. Additionally, the fractured and thermally stable eutectic structure (depicted in Fig. 3), along with precipitates that form at grain boundaries and within grains (marked in Fig. 4) during annealing process, further restricts the

movement of the grain boundaries.

Figure 6 shows the distributions of twins in the four annealed alloys. The volume fraction of the twin boundaries clearly increases during annealing. In particular, the fraction of twin boundaries increases dramatically from 7.7% after 30 min of annealing to 19.6% after 300 min of annealing.

To investigate the variation in dislocation density following different annealing durations, Fig. 7 presents the kernel average misorientation (KAM) maps and its values for the four alloys. The wrought alloy demonstrates a high degree of DRX [36], and similarly, the four annealed alloys exhibit a low dislocation density. As the annealing time increases, the dislocation density shows a slight decrease, which can be attributed to the processes of static recrystallization and grain growth occurring during annealing. Additionally, it is important to note that the majority of regions appearing in green in Fig. 7 correspond to eutectic structures, indicating that a greater accumulation of dislocations is present within the fractured eutectic regions.

Figure 8 shows the pole figures of the four annealed Zn−0.1Mg alloys. The texture type of the alloy clearly remains unchanged during annealing, whereas the strength experiences a dynamic change. Compared with that of the ECAPed alloy, the texture intensity of the alloy annealed for 1−5 min increases. When the annealing time is increased to 30 min, the texture intensity decreases to 13.79, which is lower than that of the unannealed alloy and may be related to the generation of many twins. After further annealing for 300 min, the texture intensity of the alloy increases to 28.48, which may be attributed to the preferential growth of the grains with a strong texture.

3.3 Biodegradation behaviors of annealed Zn−0.1Mg alloy

Figure 9 shows the potential dynamic polarization (PDP) curves of the ECAPed and annealed Zn−0.1Mg alloys and the variation trend diagram of the self-corrosion potential (φ_{corr}) and corrosion current density (J_{corr}) derived from the PDP

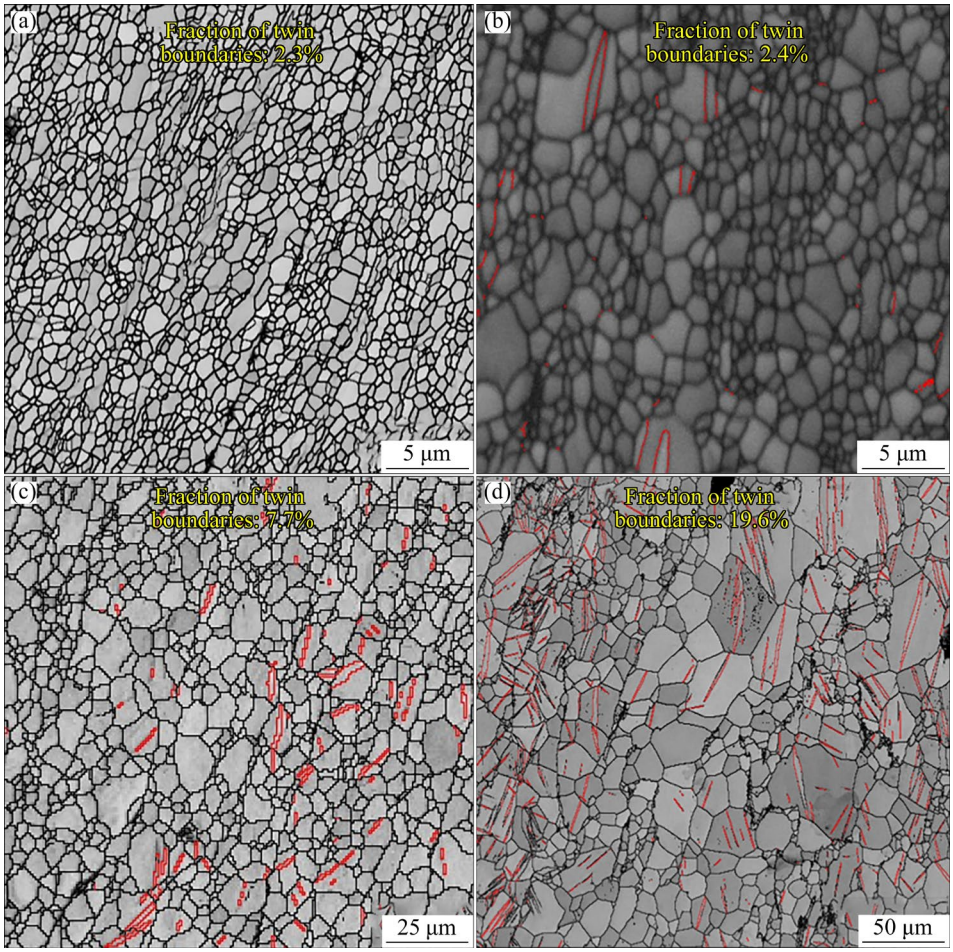

Fig. 6 Distributions of twins in four annealed Zn−0.1Mg alloys: (a) 1 min; (b) 5 min; (c) 30 min; (d) 300 min

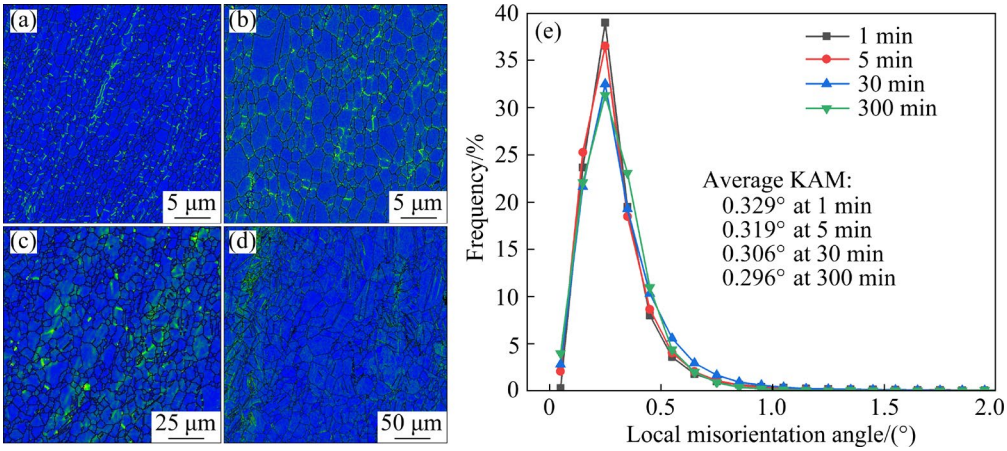

Fig. 7 KAM maps (a−d) and corresponding KAM values (e) of four annealed Zn−0.1Mg alloys: (a) 1 min; (b) 5 min; (c) 30 min; (d) 300 min

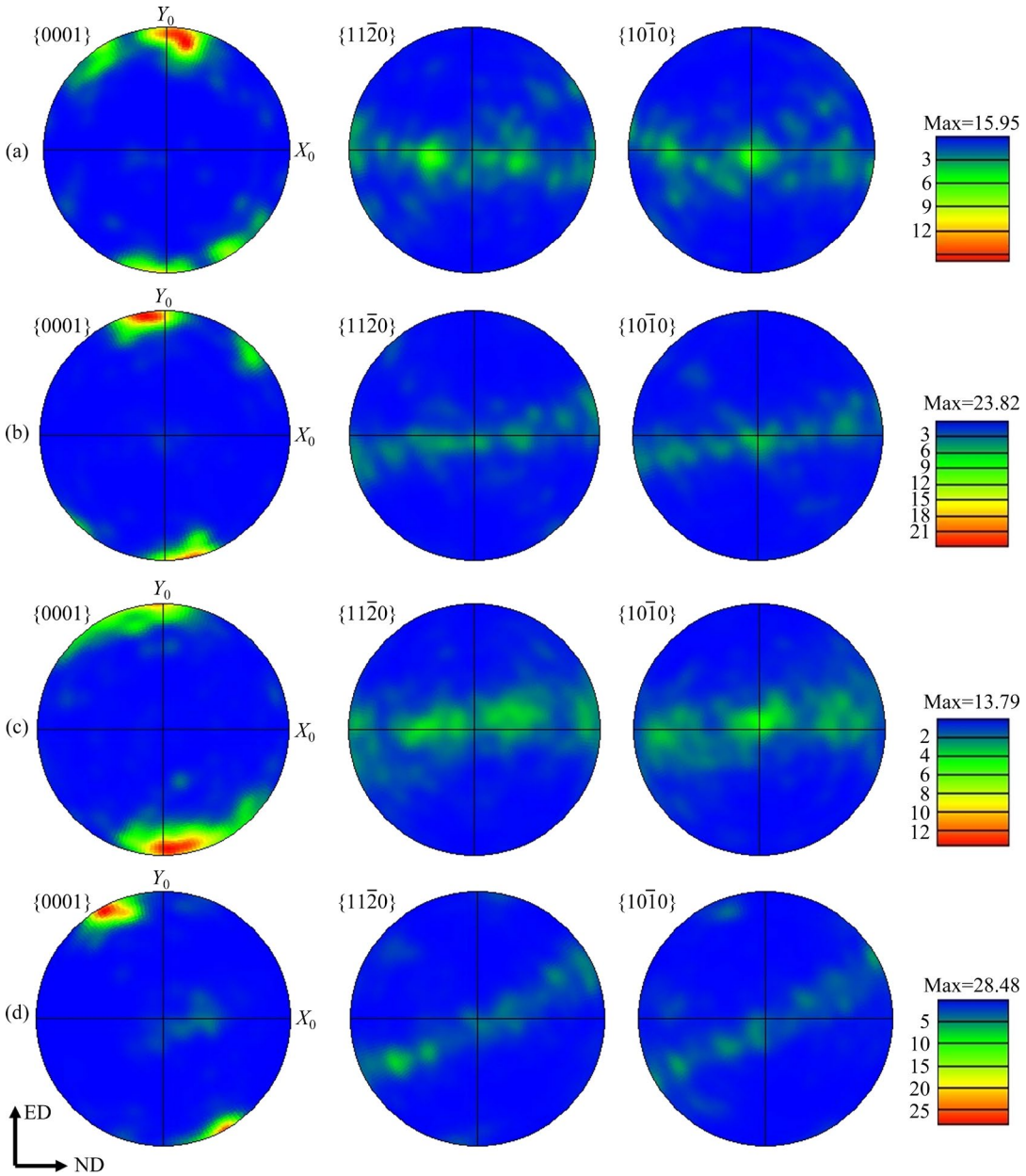

Fig. 8 Texture evolution of four annealed Zn−0.1Mg alloys: (a) 1 min; (b) 5 min; (c) 30 min; (d) 300 min

curves. The φ_{corr} value decreases with increasing annealing time, whereas the J_{corr} value clearly increases, suggesting that the corrosion resistance of the alloy decreases after annealing.

Figure 10 shows the electrochemical impedance spectroscopy (EIS) results for the ECAPed and annealed Zn−0.1Mg alloys. The Nyquist curves for all alloys exhibit two arcs of capacitive reactance across the entire frequency range. The arc in the high-frequency region is associated with the charge transfer reaction, while the arc in the low-frequency region is related to the conductivity of the electrolyte through the corrosion product film [45]. The Bode curves depicted in Fig. 10(b) indicate that the impedance values of the alloys increase from the high-frequency to the low-frequency region. Furthermore, the phase angle versus frequency plots reveal a wave crest in the high-frequency range for all alloys (Fig. 10(c)).

Furthermore, Fig. 10(d) displays the fitted equivalent circuit for the EIS data, where R_s represents the solution resistance, R_{ct} denotes the charge transfer resistance, CPE_1 indicates the double-electric layer capacitance at the electrolyte/metal interface, G (Gerischer) corresponds to the time constant of the diffusion impedance, and R_{cp} and CPE_2 refer to the resistance and capacitance of the corrosion product layer, respectively. The fitted

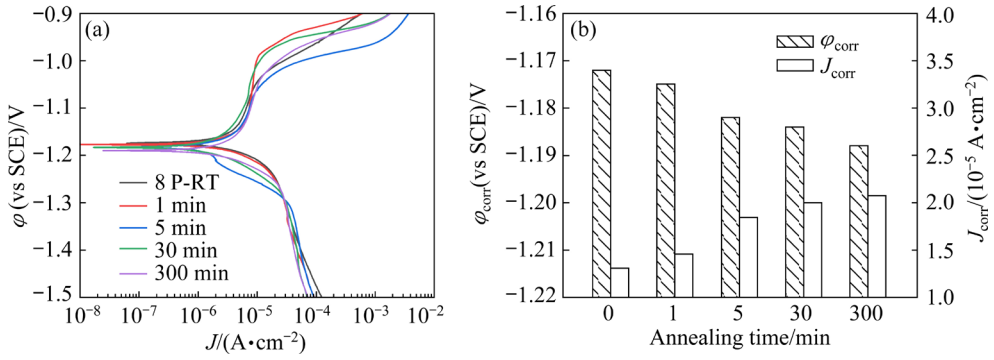

Fig. 9 (a) PDP curves of ECAPed (8 P: 8 passes) and annealed Zn−0.1Mg alloys; (b) φ_{corr} and J_{corr} versus annealing time

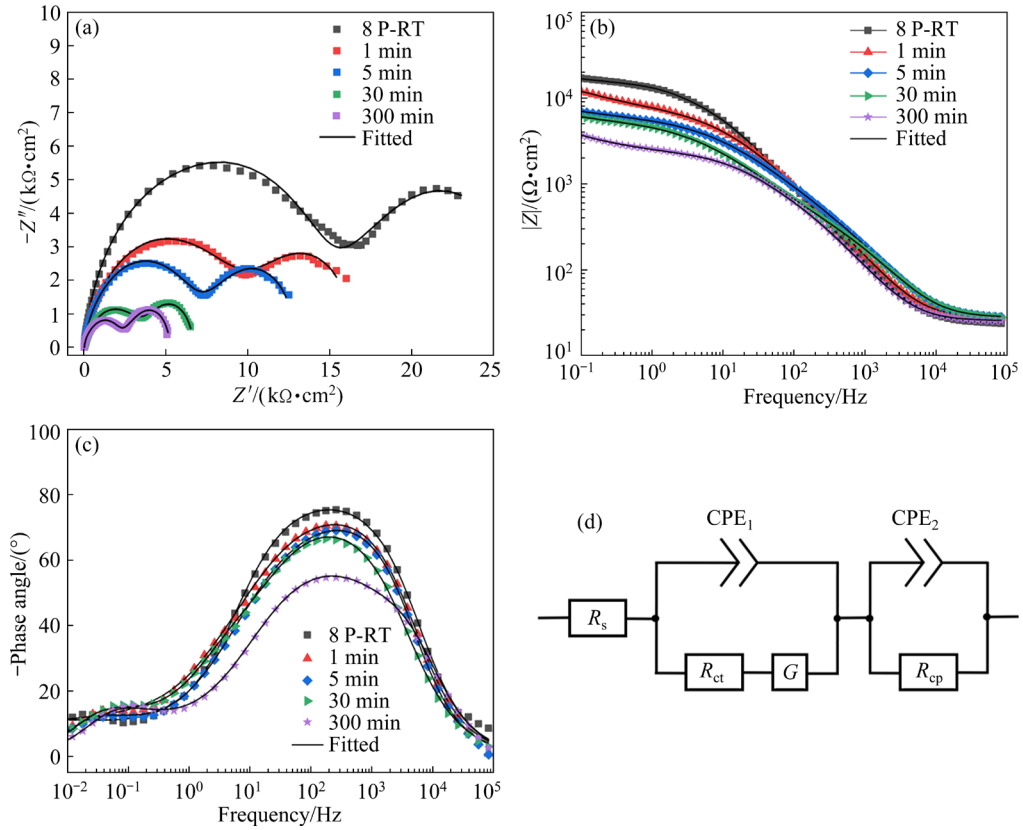

Fig. 10 EIS results of ECAPed and annealed Zn−0.1Mg alloys: (a) Nyquist plots; (b) Bode plots of $|Z|$ versus frequency; (c) Bode plots of phase angel versus frequency; (d) Equivalent circuit

values are summarized in Table 1. The R_{ct} values exhibit a clear decrease with longer annealing time, with the R_{ct} value for the sample annealed for 300 min recorded at only 2136 Ω·cm^2, about 1/3 that for the ECAPed sample. The trend observed for the CPE_2 value is inversely related to that of R_{ct}. Generally, higher R_{ct} values are associated with lower corrosion rates of the Zn matrix, while lower CPE_2 values suggest a denser alloy surface film. Consequently, the corrosion rate of the annealed alloy surpasses that of the wrought alloy, increasing further with extended annealing time, which aligns with the trend observed in the data measured by the PDP curve.

Table 2 lists the mass loss results of the wrought and annealed Zn−0.1Mg alloys after 30 d of immersion. The corrosion rate calculated from the mass loss of the annealed samples is greater than that of the wrought alloy (0.037 mm/a), which continuously increases with increasing annealing time. The immersion results demonstrate that annealing decreases the corrosion resistance of the wrought Zn−0.1Mg alloy, which is consistent with the electrochemical test results.

Figure 11 illustrates corrosion morphologies of the annealed Zn−0.1Mg alloys following a 30 d immersion in Hank's solution. Spherical corrosion products are evident on the surface of all alloys, with an increasing density observed as the annealing time extends. Furthermore, the spherical corrosion products exhibit agglomeration, resulting in a denser distribution on the surface of the alloy annealed for 300 min, indicating more extensive corrosion. To determine the specific compositions of the corrosion products, EDS analyses were performed on the alloys annealed for 5 and 300 min. The positions of the EDS analyses are indicated in Fig. 12, and the results are summarized in Table 3.

Points *A*, *B*, *D*, and *E* in Fig. 12 are associated with white granular corrosion products, while points *C* and *F* correspond to corrosion films where the accumulation of white corrosion products is absent. The corrosion products predominantly consist of Zn, Mg, Ca, C, P, and O. In the sample subjected to short-term annealing (5 min), the contents of Ca and P at point *C* are low, whereas higher levels are observed at points *A* and *B*. Notably, at point *A*, where granular corrosion products accumulate, the contents of P and Ca are measured at 7.84 wt.% and 10.44 wt.%, respectively, which can be attributed to the formation of $CaCO_3$, $Ca_3(PO_4)_2$, and $Zn_3(PO_4)_2$ [46]. With respect to the samples annealed for a long time (300 min), the Ca contents measured at points *D*, *E*, and *F* are similar, indicating the formation of large amounts of $CaCO_3$ and $Ca_3(PO_4)_2$. Compared with points *D* and *E*, *F* point has obviously lower contents of C and O but a much higher content of Zn, suggesting that more ZnO and $Zn(OH)_2$ are formed at this site. Combined with a previous study [46], it can be inferred that the corrosion products formed on

Table 1 Parameter values measured from Nyquist curves of wrought and annealed Zn−0.1Mg alloys

Annealing time/min	R_s/(Ω·cm^2)	CPE_1/μF	n_1	R_{cp}/(Ω·cm^2)	CPE_2/μF	n_2	R_{ct}/(Ω·cm^2)	G/(S·s^{n_1}·cm^{-2})
0	24.6	1.65	0.92	1397	12.6	0.55	6964	2.16×10^{-4}
1	28	2.03	0.91	1169	15.9	0.6	5514	7.31×10^{-4}
5	28.1	2.16	0.92	537	22.1	0.65	5393	7.28×10^{-4}
30	27.9	2.18	0.9	384	41.7	0.64	4946	9.10×10^{-4}
300	25.1	2.98	0.9	20	71.0	0.58	2136	9.38×10^{-4}

n_1 is the phase constant of CPE_1; n_2 is the phase constant of CPE_2

Table 2 Corrosion rates of wrought and annealed Zn− 0.1Mg alloys

Annealing time/min	Mass loss/g	Corrosion rate/(mm·a^{-1})
0 (8 P-RT)	0.0012	0.037
1	0.0014	0.042
5	0.002	0.059
30	0.0023	0.066
300	0.0024	0.069

Table 3 Compositions of corrosion products on surface of annealed Zn−0.1Mg alloys after immersion test

Annealing time/min	Location	Content/wt.%					
		Zn	Mg	C	O	P	Ca
5	*A*	34.65	1.95	10.93	34.2	7.84	10.44
	B	70.76	1.15	6.1	14.33	4.11	3.54
	C	79.77	0.85	6.42	9.22	1.78	1.96
300	*D*	8.75	1.08	8.24	42.42	14.6	24.91
	E	10.74	0.96	8.76	43.48	13.53	22.53
	F	28.6	1.06	4.61	24.82	15.34	25.58

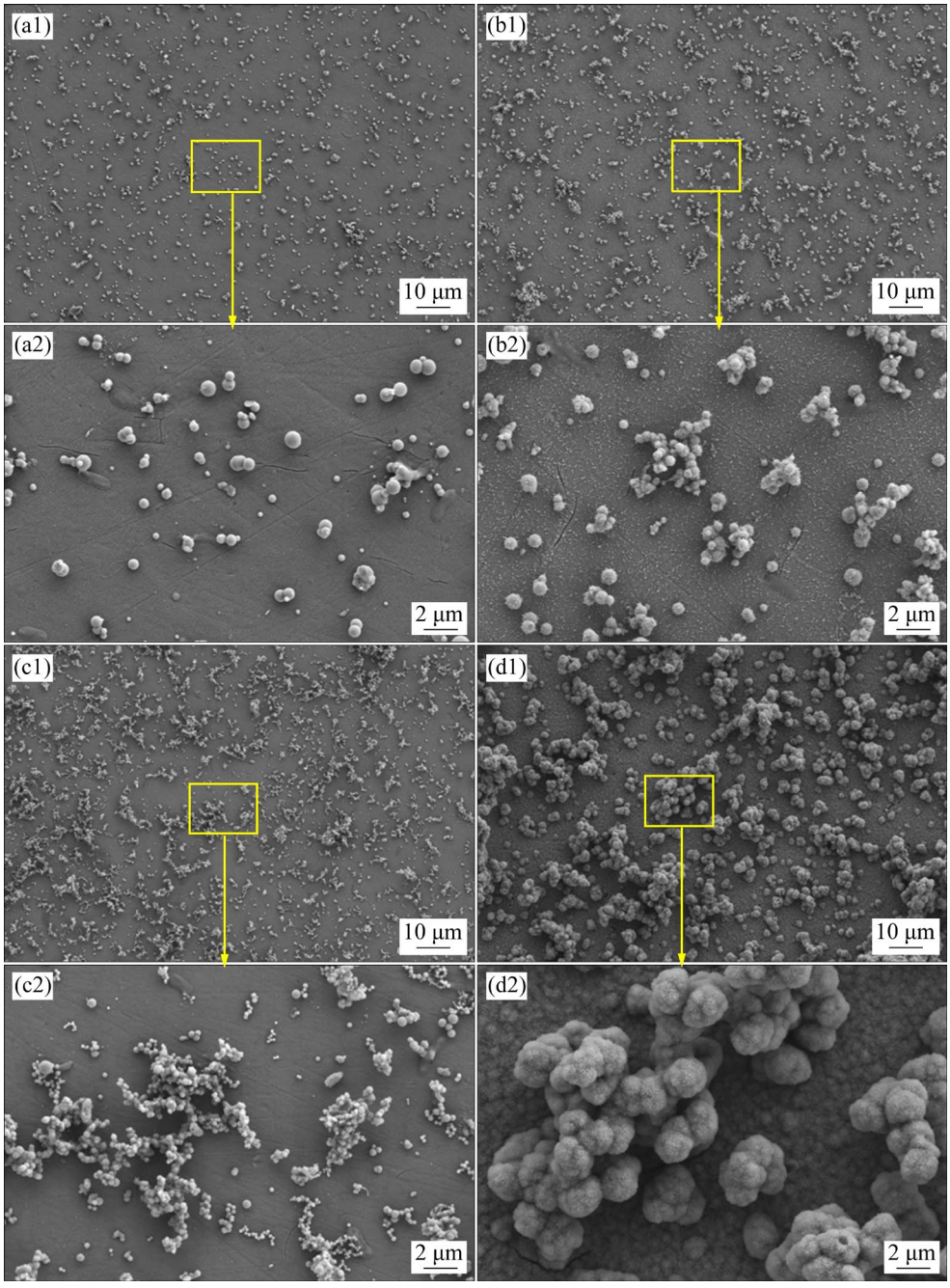

Fig. 11 Surface morphologies of annealed Zn−0.1Mg alloys after immersion for 30 d: (a1, a2) 1 min; (b1, b2) 5 min; (c1, c2) 30 min; (d1, d2) 300 min

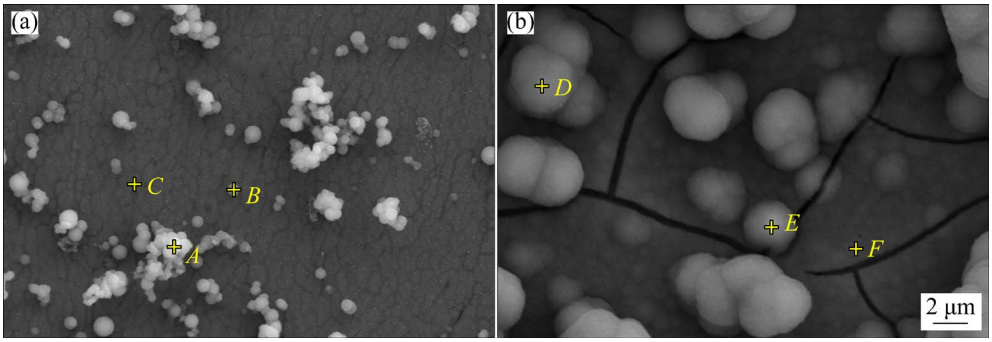

Fig. 12 Locations for EDS analysis of corrosion products on two annealed Zn−0.1Mg alloys after immersion test: (a) 5 min; (b) 300 min

Zn alloys mainly consist of $Ca_3(PO_4)_2$, $CaCO_3$, $MgCO_3$, $Mg(OH)_2$, $Zn(OH)_2$, ZnO, $Zn_3(PO_4)_2$, and $ZnCO_3$, and the white granular precipitates are mainly phosphate and calcium salts. In addition, the annealed sample (Fig. 12(b)) shows that the dense corrosion product film breaks due to internal stress or dehydration during the drying process.

Figure 13 shows SEM images of the corrosion surface of the annealed Zn−0.1Mg alloy after the removal of corrosion products. The results show that after 30 d of immersion, the alloys clearly exhibit localized corrosion. For the wrought alloy, a small amount of corrosion product along the grain boundaries is observed [36]. With increasing annealing time, the density and size of corrosion pits increase correspondingly. The alloy annealed for 300 min has the most severely corroded surface. Furthermore, corrosion mainly occurs in the eutectic structure near the grain boundaries, and further corrosion along the grain boundaries could gradually expose the Zn grains.

3.4 Influence of annealing on mechanical properties of Zn−0.1Mg alloy

The microstructure evolution of the wrought Zn−0.1Mg alloy during annealing can be summarized as follows: grain growth occurs, static precipitation of the $MgZn_2$ phase is observed, dislocation density decreases, the number of twin boundaries increases, and dynamic changes in texture intensity are noted.

After annealing, a significant reduction in the strength of the alloy is observed. Figure 1 demonstrates that the decrease in strength exceeds 200 MPa. This substantial decline may be attributed to two factors. On the one hand, static recrystallization and grain growth result in an increase in the AGS of the alloy from 1.40 to 17.84 μm after annealing, which critically compromises strength due to the weakening of fine grain strengthening [47]. Grain refinement is consistently regarded as the most effective strengthening mechanism for Zn alloys [48], a concept that also applies to Mg alloys exhibiting the same HCP structure [49]. As a consequence, the grain growth during annealing has a crucial effect on the deterioration of the strength of Zn−0.1Mg alloys. On the other hand, the variation in dislocation density is also responsible for the decreased strength. Generally, the dislocation wall and dislocation cell structure formed by dislocation accumulation and entanglement during plastic processing can easily obstruct the movement of dislocations during tensile loading and thereby improve the strength of the alloy. However, owing to static recrystallization during annealing, which consumes most of the dislocations, the density of the dislocations clearly decreases, which increases the ability of the dislocations to slip, thereby reducing the alloy strength. The influence of annealing on the mechanical properties in this study is consistent with our previous research on Zn−0.5Cu alloys [35], which revealed the same aging mechanisms for Zn alloys. In addition, although the secondary phases precipitate during annealing, they exhibit a limited strengthening effect in this work. The dispersed precipitates inside the grains are usually conducive to improving the strength of metallic materials [50]. However, it is evident from Fig. 4 that the precipitates within the grains are not dispersed but are concentrated to a large degree. This phenomenon increases the probability of crack initiation and weakens the dispersion strengthening effect, which is insufficient to compensate for the strength reduction caused by grain coarsening.

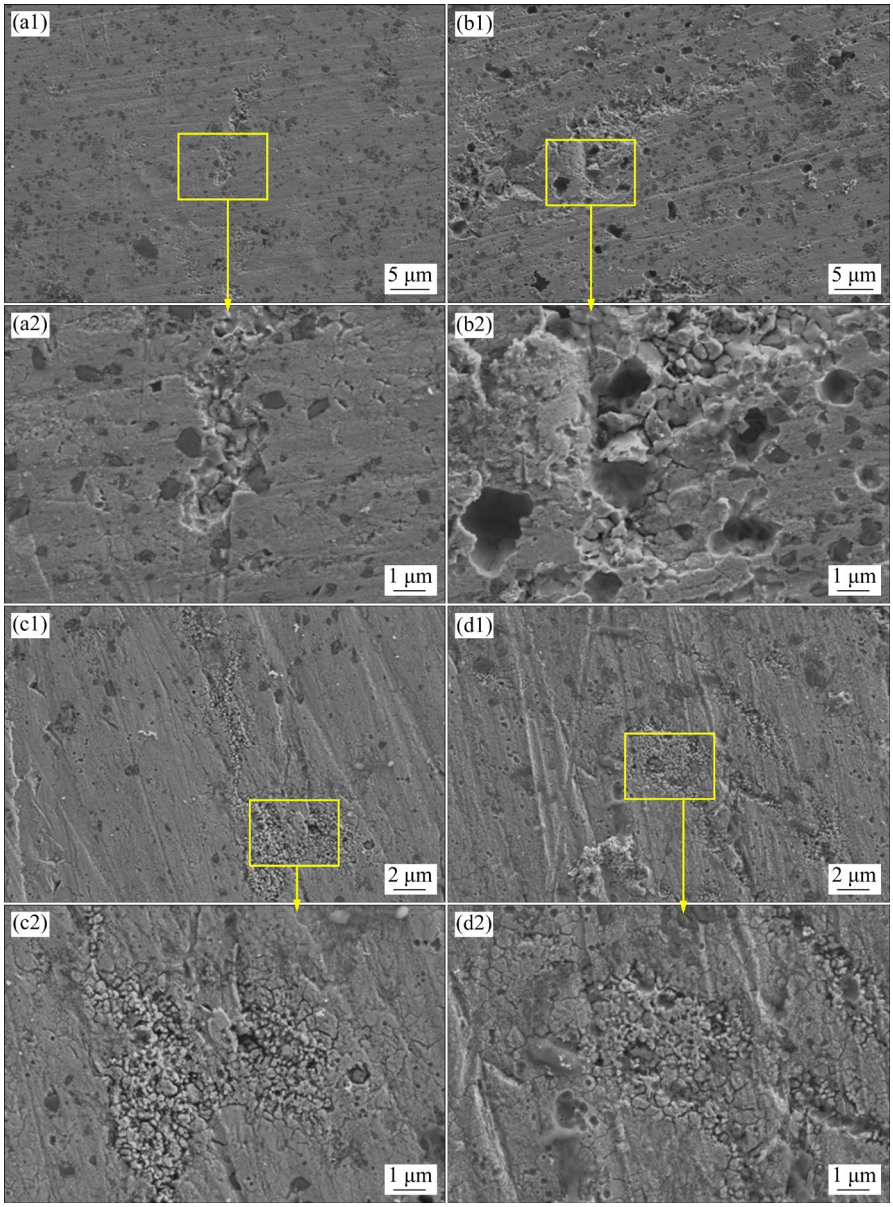

Fig. 13 SEM images of annealed Zn−0.1Mg alloys after immersion tests and removal of corrosion products: (a1, a2) 1 min; (b1, b2) 5 min; (c1, c2) 30 min; (d1, d2) 300 min

The ductility of the alloy exhibits fluctuations as the annealing time increases. Figure 1 indicates that after 1−5 min of annealing, the elongation of the alloy first declines and then returns to its initial state after 30 min of annealing. However, a further decrease in elongation is noted after 300 min of annealing. Notably, an unusual increase occurs within annealing time range of 30−120 min. The variations in elongation during the annealing process are primarily linked to changes in the grain size, precipitates, texture, and presence of annealing twins. Following annealing, the increase in the grain size inhibits grain boundary sliding, which reduces the elongation. Additionally, the quantity of secondary phase particles at the grain boundaries rises during annealing. These intergranular precipitates weaken the grain boundaries and contribute to the stress concentrations during tensile testing, which can lead to the rapid microcrack initiation and a subsequent reduction in ductility [51].

Compared with the annealed Zn−0.5Cu alloy [35], the Zn−0.1Mg alloy exhibited an abnormal increase in ductility from 30 to 120 min of annealing. The abnormal increase in elongation of the alloy after 30 min of annealing is related mainly to the annealing twinning and weakened texture. On the one hand, texture weakening is a common and effective strategy to increase the plasticity of HCP

alloys [39]. WANG et al [52] reported that torsion and annealing treatments improved the ductility of alloys through the texture weakening and grain refinement. Similarly, WU et al [53] reported a significant improvement in plasticity for a hot-rolled Mg−1Gd alloy owing to the weakened texture during annealing. In this study, the intensity of the texture first increases after annealing the alloy for 1−5 min, whereas the texture weakening phenomenon occurs after annealing for 30 min, which can be one reason for the abnormal increase in elongation of the alloy. On the other hand, the ductility of the wrought Zn−0.1Mg alloy is dominated mainly by dislocation slip due to a lack of enough activated slip systems in the HCP structure. Therefore, as a unique deformation mode, twinning can cooperate with slip systems to improve the ductility of the alloy [54]. When the annealing time increases to 30 min, the proportion of twins in the alloy clearly increases. The reorientation of twins and the decreased CRSS could activate the ⟨*c*+*a*⟩ slip systems, thereby improving the ductility of the alloy. Figure 14 clearly shows that the average Schmid factors of nonbasal slip systems increase in the alloy annealed for 30 min.

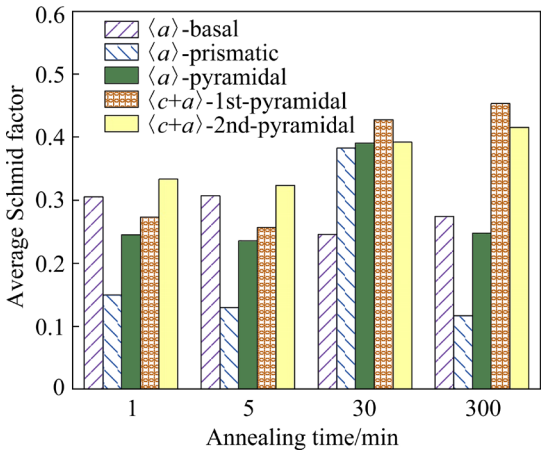

Fig. 14 Average Schmid factors for diverse slip systems of annealed alloys

Finally, when the annealing period was increased to 300 min, the grains obviously grew, and the increased texture intensity combined to cause a rapid decrease in the ductility of the alloy. Although the content of twins in the alloy annealed for 300 min is the highest, their contribution to elongation is reduced. SHEN et al [55] reported that twins in the AZ31 Mg alloy increased, but the ductility apparently decreased due to an increase in the spacing between twins.

3.5 Influence of annealing on corrosion behavior of Zn−0.1Mg alloy

Both electrochemical testing and immersion mass loss analyses reveal that annealing reduces the corrosion resistance of the Zn−0.1Mg alloy, with this deterioration becoming severer with longer annealing time. In conjunction with microstructure characterization, it can be suggested that the corrosion behavior of the annealed alloys is predominantly influenced by factors such as the grain size, secondary phases, and twins.

The influence of the grain size on the corrosion resistance of metallic materials remains a subject of debate. Typically, the corrosion rate of Zn alloys decreases with grain refinement due to reduced kinetics of the anode and cathode reactions [56]. However, as Zn grains are refined, the density of grain boundaries increases, which can enhance the likelihood of intergranular corrosion and accelerate the overall corrosion of the alloy [57]. Generally, although grain refinement tends to improve corrosion resistance, it can also lead to increased grain boundary density, which facilitates intergranular corrosion. Most studies [58,59] indicate that plastic deformation processing enhances the corrosion resistance of metallic materials through grain refinement. Refined grains increase grain boundary density, which can hinder corrosion propagation by serving as a physical barrier [58]. Additionally, grain refinement aids in the formation of continuous protective corrosion product films, effectively isolating the matrix from corrosive environments [59]. In this study, considering the evolution of grain size and corrosion behavior with extended annealing time, it is evident that ECAP refines the alloy grains and enhances corrosion resistance, while annealing decreases this beneficial effect by coarsening the grains [60].

For the impact of secondary phases, the eutectic structure containing Zn + Mg_2Zn_{11} phases has a higher self-corrosion potential than the Zn matrix, which induces galvanic corrosion and is usually the cause of corrosion (Fig. 13) [61]. In comparison to the ECAPed alloy, the annealed alloy exhibits a significant quantity of $MgZn_2$ precipitates that are formed within the grains and at the boundaries. The amount and size of these $MgZn_2$ precipitates are observed to increase with prolonged annealing duration. Given that the $MgZn_2$ phase possesses a higher self-corrosion potential than the Zn

matrix [62], a potential difference is established between the two phases, resulting in galvanic corrosion. Typically, the $MgZn_2$ phase acts as the anode during galvanic corrosion, and the enlargement of its size due to annealing enhances the area of the active anode, thereby accelerating the corrosion process.

Additionally, a pertinent study indicated that the presence of twins intensified intercrystalline corrosion, resulting in decreased corrosion resistance [54]. As the annealing time increases, the proportion of twins in the annealed Zn−0.1Mg alloy rises, which may establish microelectric couples with the Zn matrix, thereby accelerating corrosion. Consequently, the rise in the number of twins during the annealing process may also contribute to the reduction in corrosion resistance.

4 Conclusions

(1) The tensile strength of the wrought Zn−0.1Mg alloy experiences a rapid and significant decrease with longer annealing time, falling from a UTS of 383 MPa for the ECAPed alloy to 102 MPa for the alloy annealed for 1440 min. Ductility exhibits fluctuating changes and ultimately declines sharply after extended annealing.

(2) The corrosion rate of the alloy increases gradually with increasing annealing time, from 0.037 mm/a for the ECAPed alloy to 0.069 mm/a for the 300 min-annealed sample. The decreased corrosion resistance can be attributed to the grain growth, increased precipitates and formation of twins after annealing.

(3) The monotonically reduced strength of the alloy with prolonged annealing time is caused mainly by coarsening and decreased dislocation density. The deterioration of ductility is associated with the grain growth and increased texture intensity, whereas the abnormal improvement in ductility during 30−120 min of annealing originates from the generation of twinning.

(4) This study provides new insights into aging mechanisms and the design and application of high-performance biodegradable Zn alloys tailored for specific biomedical needs. Future research should concentrate on two key aspects: optimizing annealing conditions to achieve a suitable balance between the mechanical properties and corrosion rates of Zn alloys for particular applications; addressing the aging issues of Zn alloys to enable broader applications.

CRediT authorship contribution statement

Huan LIU: Conceptualization, Funding acquisition, Supervision, Writing − Review & editing; **Li-feng YE:** Data curation, Investigation, Writing − Original draft; **Jing-bo LI:** Data curation, Writing − Original draft; **Chao SUN:** Methodology, Validation; **Yu-na WU:** Methodology, Visualization; **Jia JU:** Methodology, Visualization; **Hang TENG:** Methodology; **Jing-hua JIANG:** Conceptualization, Writing − Review & editing; **Jing BAI:** Funding acquisition, Methodology, Project administration; **Feng XUE:** Methodology.

Declaration of competing interest

The authors declare that they have no known competing financial interests or personal relationships that could have appeared to influence the work reported in this paper.

Data availability

The raw or processed data required to reproduce these findings are available from the corresponding author by request.

Acknowledgments

This work was supported by the National Natural Science Foundation of China (No. 52271101), Suzhou Science and Technology Project, China (Nos. SYG202312, SJC2023005, SZS2023023), Nanjing Major Science and Technology Project, China (No. 202309015), and the Opening Project of Jiangsu Key Laboratory of Advanced Structural Materials and Application Technology, China (No. ASMA202305).

References

[1] KE Gui-zhou, YUE Rui, HUANG Hua, KANG Bin, ZENG Hui, YUAN Guang-yin. Effects of Sr addition on microstructure, mechanical properties and in vitro degradation behavior of as-extruded Zn−Sr binary alloys [J]. Transactions of Nonferrous Metals Society of China, 2020, 30: 1873−1883.

[2] VIDA T A, SILVA C A P, LIMA T S, CHEUNG N, BRITO C, GARCIA A. Tailoring microstructure and microhardness of Zn−1wt.%Mg−(0.5wt.%Mn, 0.5wt.%Ca) alloys by solidification cooling rate [J]. Transactions of Nonferrous Metals Society of China, 2021, 31: 1031−1048.

[3] JIA Bo, YANG Hong-tao, HAN Yu, ZHANG Ze-chuan, QU Xin-hua, ZHUANG Yi-fu, WU Qiang, ZHENG Yu-feng, DAI Ke-rong. In vitro and in vivo studies of Zn−Mn biodegradable metals designed for orthopedic applications [J]. Acta Biomaterialia, 2020, 108: 358−372.

[4] KAFRI A, OVADIA S, YOSAFOVICH-DOITCH G, AGHION E. In vivo performances of pure Zn and Zn−Fe alloy as biodegradable implants [J]. Journal of Materials Science, 2018, 29: 1−8.

[5] BAO Guo, WANG Kun, YANG Li-jun, HE Jia-ling, HE Bin, XU Xiao-xue, ZHENG Yu-feng. Feasibility evaluation of a Zn−Cu alloy for intrauterine devices: In vitro and in vivo studies [J]. Acta Biomaterialia, 2022, 142: 374−387.

[6] WANG Xiang, SHAO Xiao-xi, DAI Tai-qiang, XU Fang-fang, ZHOU J G, QU Gong-qi, TIAN Lei, LIU Bin, LIU Yan-pu. In vivo study of the efficacy, biosafety, and degradation of a zinc alloy osteosynthesis system [J]. Acta Biomaterialia, 2019, 92: 351−361.

[7] LI Guan-nan, YANG Hong-tao, ZHENG Yu-feng, CHEN Xie-Hui, YANG Jian-an, ZHU Dong-hui, RUAN Li-qun, TAKASHIMA K. Challenges in the use of zinc and its alloys as biodegradable metals: Perspective from biomechanical compatibility [J]. Acta Biomaterialia, 2019, 97: 23−45.

[8] ZHU Su-ming, WU Cheng-cheng, LI Guan-nan, ZHENG Yu-feng, NIE Jian-feng. Creep properties of biodegradable Zn−0.1Li alloy at human body temperature: Implications for its durability as stents [J]. Materials Research Letters, 2019, 7(9): 347−353.

[9] BOWEN P K, SHEARIER E R, ZHAO S, GUILLORY R J II, ZHAO F, GOLDMAN J, DRELICH J W. Biodegradable metals for cardiovascular stents: from clinical concerns to recent Zn-alloys [J]. Advanced Healthcare Materials, 2016, 5: 1121−1140.

[10] NIU Kun-ning, ZHANG De-chuang, QI Fu-gang, LIN Jian-guo, DAI Yi-long. Achieving high strength and antibacterial Zn−4Ag−Mn alloy with homogenous corrosion behavior via high-pressure solid solution [J]. Transactions of Nonferrous Metals Society of China, 2024, 34: 2231−2244.

[11] ZHANG Jing-dan, ZHU Xing-long, GUO Pu-shan, ZHANG Yi, XU Ding-yang, PANG Yuan, SONG Zhen-lun, YANG Li-jing. Effects of Li addition on the properties of biodegradable Zn−Fe−Li alloy: Microstructure, mechanical properties, corrosion behavior, and cytocompatibility [J]. Materials Today Communications, 2024, 39: 108661.

[12] YANG Hong-tao, JIA Bo, ZHANG Ze-chuan, QU Xin-hua, LI Guan-nan, LIN Wen-jiao, ZHU Dong-hui, DAI Ke-rong, ZHENG Yu-feng. Alloying design of biodegradable zinc as promising bone implants for load-bearing applications [J]. Nature Communications, 2020, 11: 401.

[13] LIU Xi-wei, SUN Jian-ke, QIU Ke-jin, YANG Ying-hong, PU Zhong-jie, LI Li, ZHENG Yu-feng. Effects of alloying elements (Ca and Sr) on microstructure, mechanical property and in vitro corrosion behavior of biodegradable Zn−1.5Mg alloy [J]. Journal of Alloys and Compounds, 2016, 664: 444−452.

[14] DUAN Jing-zhu, LI Lei, LIU Cong-fu, SUO Yu-song, WANG Xiang-jie, YANG Yang. Novel Zn−2Cu−0.2Mn−*x*Li (*x*=0, 0.1 and 0.38) alloys developed for potential biodegradable implant applications [J]. Journal of Alloys and Compounds, 2022 916: 165478.

[15] HUANG He, LIU Huan, REN Kang-xuan, SHI Jia-hui, JU Jia, WU Hao-ran, JIANG Jing-hua, MA Ai-bin, XUE Feng, BAI Jing, ZHENG Yu-feng. Improvement of ductility and work hardening ability in a high strength Zn−Mg−Y alloy via micron-sized and submicron-sized YZn_{12} particles [J]. Journal of Alloys and Compounds, 2021, 877: 160268.

[16] LI Zhen, SHI Zhang-zhi, HAO Yuan, LI Hua-fang, LIU Xue-feng, VOLINSKY A A, ZHANG Hai-jun, WANG Lu-ning. High-performance hot-warm rolled Zn−0.8Li alloy with nano-sized metastable precipitates and sub-micron grains for biodegradable stents [J]. Journal of Materials Science & Technology, 2019, 35: 2618−2624.

[17] LI Rui-min, DING Yu-tian, ZHANG Hong-fei, LEI Jian, SHEN Yue. Effective strengthening and toughening in Zn−1Mg alloy with bimodal grain structure achieved by conventional extrusion [J]. Materials Science and Engineering A, 2022, 854: 143850.

[18] SHI Zhang-zhi, YU Jing, LIU Xue-feng. Microalloyed Zn−Mn alloys: From extremely brittle to extraordinarily ductile at room temperature [J]. Materials & Design, 2018, 144: 343−352.

[19] MOSTAED E, ARDAKANI M S, SIKORA-JASINSKA M, DRELICH J W. Precipitation induced room temperature superplasticity in Zn−Cu alloys [J]. Materials Letters, 2019, 244: 203−206.

[20] BEDNARCZYK W, KAWAŁKO J, RUTKOWSKI B, WĄTROBA M, GAO N, STARINK M J, BAŁA P, LANGDON T G. Abnormal grain growth in a Zn−0.8Ag alloy after processing by high-pressure torsion [J]. Acta Materialia, 2021, 207: 116667.

[21] MOLLAEI N, RAZAVI S H, ABOUTALEBI M R, FATEMI S M. Effect of Mn addition on the microstructure, mechanical, and corrosion properties of an extruded biodegradable Zn−0.2Mg alloy [J]. Journal of Materials Research and Technology, 2023, 22: 1983−1998.

[22] ZHANG Xi-yuan, LIU Gui-sen, JIANG Lin-feng, JIAO Dian, JIANG Ji-miao, CHEN Chun, GAO Zhi-qiang, NIU Jia-lin, SHA Gang, SHEN Yao, HUANG Hua, YUAN Guang-yin. Hierarchical structured Zn−Cu−Li alloy with high strength and ductility and its deformation mechanisms [J]. International Journal of Plasticity, 2023, 169: 103731.

[23] ZHENG Li, ZHANG Shi-hong, HELM D, SONG Hong-wu, SONG Guang-sheng, YE Neng-yong. Twinning and detwinning during compression-tension loading measured by quasi in situ electron backscatter diffraction tracing in Mg−3Al−Zn rolled sheet [J]. Rare Metals, 2015, 34: 698−705.

[24] WANG Dong, GAO Chong, LUO Hong-yun, YANG Yong-hong, MA Yue. Texture evolution behavior and anisotropy of 2A97 Al−Li alloy during recrystallization at elevated temperature [J]. Rare Metals, 2023, 42: 3139−3149.

[25] LI Zhi-peng, ZHANG Jian-fei, ZHAI Ya-di, ZHANG Jia-bao, WANG Xiao-dong, ZHANG Ze, MAO Sheng-cheng, HAN Xiao-dong. Dynamic mechanisms of strengthening and softening of coherent twin boundary via dislocation pile-up and cross-slip [J]. Materials Research Letters, 2022, 10: 539−546.

[26] ECOB N, RALPH B. The effect of grain size on deformation twinning in a textured zinc alloy [J]. Journal of Materials Science, 1983, 18: 2419−2429.

[27] REN Kang-xuan, ZHANG Kai-xiao, ZHANG Yue, JU Jia, YAN Kai, JIANG Jing-hua, MA Ai-bin, XUE Feng, BAI Jing, LIU Huan. Effect of ECAP temperature on formation of triple heterogeneous microstructure and mechanical properties of Zn−1Cu alloy [J]. Materials Science and Engineering A, 2021, 826: 141990.

[28] CLAUDIA G M, IVAN G, LAIA O M, EMILIO J P, MARIA-PAU G, MAURIZIO V, JOSÉ LUÍS C, MARTA P. Influence of ECAP process on mechanical, corrosion and bacterial properties of Zn−2Ag alloy for wound closure devices [J]. Materials & Design, 2023, 228: 111817.

[29] WANG Xiu-ping, MA Yan, MENG Bao, WAN Min. Effect of equal-channel angular pressing on microstructural evolution, mechanical property and biodegradability of an ultrafine-grained zinc alloy [J]. Materials Science and Engineering A, 2021, 824: 141857.

[30] LIU Huan, YE Li-feng, REN Kang-xuan, SUN Chao, ZHUO Xiao-ru, YAN Kai, JU Jia, JIANG Jing-hua, XUE Feng, BAI Jing. Evolutions of $CuZn_5$ and Mg_2Zn_{11} phases during ECAP and their impact on mechanical properties of Zn−Cu−Mg alloys [J]. Journal of Materials Research and Technology, 2022, 21: 5032−5044.

[31] LI Rui-min, DING Yu-tian, ZHANG Hong-fei, WANG Xue, GAO Yu-bi, XU Jia-yu. Toward high strength and large strain hardening Zn alloys via a novel multiscale-heterostructure strategy [J]. Materials Science and Engineering A, 2024, 899: 146410.

[32] ARDAKANI M S, MOSTAED E, SIKORA-JASINSKA M, KAMPE S L, DRELICH J W. The effects of alloying with Cu and Mn and thermal treatments on the mechanical instability of Zn−0.05Mg alloy [J]. Materials Science and Engineering A, 2020, 770: 138529.

[33] JIN H L, ZHAO S, GUILLORY R, BOWEN P K, YIN Z Y, GRIEBEL A, SCHAFFER J, EARLEY E J, GOLDMAN J, DRELICH J W. Novel high-strength, low-alloys Zn−Mg (<0.1 wt.% Mg) and their arterial biodegradation [J]. Materials Science and Engineering C, 2018, 84: 67−79.

[34] XU Zi-yue, LIU Huan, REN Kang-xuan, SUN Chao, ZHUO Xiao-ru, YAN Kai, JU Jia, XUE Feng, BAI Jing, JIANG Jing-hua. Revealing the abnormal softening mechanisms of Zn−xCu (x=2, 3) wrought alloys by gradually increasing ECAP numbers [J]. Materials Science and Engineering A, 2022, 856: 143962.

[35] YE Li-feng, SUN Chao, ZHUO Xiao-ru, LIU Huan, JU Jia, XUE Feng, BAI Jing, JIANG Jing-hua, XIN Yun-chang. Evolution of grain size and texture of Zn−0.5Cu ECAP alloy during annealing at 200 ℃ and its impact on mechanical properties [J]. Journal of Alloys and Compounds, 2022, 919: 165871.

[36] YE Li-feng, LIU Huan, SUN Chao, ZHUO Xiao-ru, JU Jia, XUE Feng, BAI Jing, JIANG Jing-hua, XIN Yun-chang. Achieving high strength, excellent ductility, and suitable biodegradability in a Zn−0.1Mg alloy using room-temperature ECAP [J]. Journal of Alloys and Compounds, 2022, 926: 166906.

[37] WANG Zi-hao, SONG Jian, PENG Ye-ping. New insights and perspectives into biodegradable metals in cardiovascular stents: A mini review [J]. Journal of Alloys and Compounds, 2024, 1002: 175313.

[38] SHIRI M, JAFARI H, SINGH R. Effect of extrusion parameters on degradation of magnesium alloys for bioimplant applications: A review [J]. Transactions of Nonferrous Metals Society of China, 2022, 32(9): 2787−2813.

[39] LI Feng, CHENG Wei-li, YU Hui, WANG Hong-xia, NIU Xiao-feng, WANG Li-fei, LI Hang, HOU Hua. Corrosion behavior and mechanical properties of extruded low-alloyed Mg−0.5Bi−0.5Y−0.2Zn alloy [J]. Transactions of Nonferrous Metals Society of China, 2023, 33(3): 743−754.

[40] XU Ya-nan, WANG Wei-qiang, YU Feng-yun, YANG Shuai-kang, YUAN Yong-hui, WANG Yi-nong. The enhancement of mechanical properties and uniform degradation of electrodeposited Fe−Zn alloys by multilayered design for biodegradable stent applications [J]. Acta Biomaterialia, 2023, 161: 309−323.

[41] ZHANG Zhi, XIE Jin-shu, ZHANG Jing-huai, DONG Hao, LIU Shu-juan, ZHANG Xiao-bo, WANG Jun, WU Rui-zhi. Simultaneously improving mechanical and anti-corrosion properties of extruded Mg−Al dilute alloy via trace Er addition [J]. Journal of Materials Science & Technology, 2023, 150: 49−64.

[42] XIE Dong-sheng, PAN Hu-cheng, PAN Zhen, FU Tong, ZENG Zhuo-ran, XIE Hong-bo, REN Yu-ping, TANG Wei-neng, QIN Gao-wu. Achieving outstanding heat-resistant properties in Mg alloy via constructing stable solute-network [J]. Materials Research Letters, 2023, 11: 374−382.

[43] SHI Zhang-zhi, GAO Xi-xian, ZHANG Hai-jun, LIU Xue-feng, LI Hui-yan, ZHOU Chao, YIN Yu-xia, WANG Lu-ning. Design biodegradable Zn alloys: Second phases and their significant influences on alloy properties [J]. Bioactive Materials, 2020, 5: 210−218.

[44] WĄTROBA M, BEDNARCZYK W, KAWAŁKO J, BAŁA P. Effect of zirconium microaddition on the microstructure and mechanical properties of Zn−Zr alloys [J]. Materials Characterization, 2018, 142: 187−194.

[45] XIE Jin-shu, ZHANG Jing-huai, ZHANG Zhi, YU Zi-jian, XU Zhi-hao, WANG Ru, FANG Da-qing, ZHANG Xiao-bo, ZHANG Xiao-ru, WU Rui-zhi. Corrosion mechanism of Mg alloys involving elongated long period stacking ordered phase and intragranular lamellar structure [J]. Journal of Materials Science & Technology, 2023, 151: 190−203.

[46] CAO Meng, SHI Zhang-zhi, SUN Jin-ling, LI Zhen, WANG Lu-ning. Three-stage degradation behavior and dealloying assisted galvanic corrosion mechanism of 300 MPa grade Zn−2Cu−xLi (x=0.2−0.8) alloys in simulated body fluid [J]. Corrosion Science, 2024, 228: 111818.

[47] ZHANG Yu-xiu, XIAO Zhen-yu, HUO Qing-huan, ZHANG Zhi-rou, TANG Jiao, AKI H, YANG Xu-yue. Effects of pre-compression on the three-dimensional creep anisotropy of a hot-rolled Mg−4wt.%Y binary alloy sheet [J]. Materials Science and Engineering A, 2020, 772: 138843.

[48] ZHANG Yu, YAN Yang, XU Xue-mei, LU Yu-jiao, CHEN Liang-jian, LI Ding, DAI Yi-long, KANG Yi-jun, YU Kun. Investigation on the microstructure, mechanical properties, in vitro degradation behavior and biocompatibility of newly developed Zn−0.8%Li−(Mg,Ag) alloys for guided bone regeneration [J]. Materials Science and Engineering C, 2019, 99: 1021−1034.

[49] SUN Chao, LIU Huan, XU Zi-yue, WU Yu-na, YAN Kai, JU Jia, JIANG Jing-hua, XUE Feng, BAI Jing, XIN Yun-chang. Refining 18R-LPSO phase into sub-micron range by pre-kinking design and its prominent strengthening effect on $Mg_{97}Y_2Zn_1$ alloy [J]. Journal of Materials Science & Technology, 2024, 176: 13−24.

[50] CHEN Hong-can, XIE Tian-ci, LIU Quan, HUANG Yuan-ding, LIU Bin, LUO Qun, LI Qian. Mechanism and prediction of aging time related thermal conductivity evolution of

Mg−Zn alloys [J]. Journal of Alloys and Compounds, 2023, 930: 167392.
[51] MOHAMED A , WANG Y C, PEDRO H R P, HUANG Y, WANG Y W, CHENG X W, LI S K, LANGDON T G. Effect of heat treatments on the microstructures and tensile properties of an ultrafine-grained Al−Zn−Mg alloy processed by ECAP [J]. Journal of Alloys and Compounds, 2018, 749: 567−574.
[52] WANG Jun, YANG Xu-yue, LI Yi, XIAO Zhen-yu, ZHANG Du-xiu, SAKAI T. Enhanced ductility and reduced asymmetry of Mg−2Al−1Zn alloy plate processed by torsion and annealing [J]. Transactions of Nonferrous Metals Society of China, 2015, 25: 3928−3935.
[53] WU W X, JIN L, WANG F H, SUN J, ZHANG Z Y, DING W J, DONG J. Microstructure and texture evolution during hot rolling and subsequent annealing of Mg−1Gd alloy [J]. Materials Science and Engineering A, 2013, 582: 194−202.
[54] LI Lian-hui, LIU Wen-hong, QI Fu-gang, WU Di, ZHANG Zhi-qiang. Effects of deformation twins on microstructure evolution, mechanical properties and corrosion behaviors in magnesium alloys—A review [J]. Journal of Magnesium and Alloys, 2022, 10: 2334−2353.
[55] SHEN Tian-yuan, LIU Huan, YANG Gong-ji, MA Min, JIANG Bing-chun, JING Lei, WANG Xiao-jun, TANG Lun-yuan, LU Li-wei. Influence of cryogenic treatment time on the mechanical properties of AZ31 magnesium alloy sheets after cross-rolling [J]. Journal of Alloys and Compounds, 2024, 986: 174096.
[56] LI Mou-cheng, JIANG Li-li, ZHANG Wen-qi, QIAN Yu-hai, LUO Su-zhen, SHEN Jia-nian. Electrochemical corrosion behavior of nanocrystalline zinc coatings in 3.5% NaCl solutions [J]. Journal of Solid State Electrochemistry, 2007, 11: 1319−1325.
[57] SUN Chao, LIU Huan, WANG Ce, JU Jia, WANG Guo-wei, JIANG Jing-hua, MA Ai-bin, BAI Jing, XUE Feng, XIN Yun-chang. Anisotropy investigation of an ECAP-processed Mg−Al−Ca−Mn alloy with synergistically enhanced mechanical properties and corrosion resistance [J]. Journal of Alloys and Compounds, 2022, 911: 165046.
[58] BIRBILIS N, RALSTON K D, VIRTANEN S, FRASER H L, DAVIES C H J. Grain character influences on corrosion of ECAPed pure magnesium [J]. Corrosion Engineering, Science and Technology, 2010, 45(3): 224−230.
[59] WU Peng-peng, XU Fang-jun, DENG Kun-kun, HAN Fu-yin, ZHANG Zhong-zhong, GAO Rui. Effect of extrusion on corrosion properties of Mg−2Ca−xAl (x=0, 2, 3, 5) alloys [J]. Corrosion Science, 2017, 127: 280−290.
[60] ZHAO Ming-chun, LIU Ming, SONG Guang-ling, ATRENS A. Influence of the β-phase morphology on the corrosion of the Mg alloy AZ91[J]. Corrosion Science, 2008, 50(7): 1939−1953.
[61] CAO Fu-yong, SHI Zhi-ming, SONG Guang-ling, LIU Ming, ANDREJ A. Corrosion behaviour in salt spray and in 3.5% NaCl solution saturated with $Mg(OH)_2$ of as-cast and solution heat-treated binary Mg−X alloys: X=Mn, Sn, Ca, Zn, Al, Zr, Si, Sr [J]. Corrosion Science, 2013, 76: 60−97.
[62] BYUN Jong-min, YU Ji-min, KIM D K, KIM T Y, JUNG W S, KIM D Y. Corrosion behavior of Mg_2Zn_{11} and $MgZn_2$ single phases [J]. Journal of Korean Institute of Metal and Materials, 2013, 51: 413−419.

退火处理对高性能变形 Zn−0.1Mg 合金组织、力学性能和生物降解行为的影响

刘 欢[1]，叶李凤[1,2]，李静波[1]，孙 超[3]，吴玉娜[1]，巨 佳[4]，滕 航[5]，江静华[1,6]，白 晶[3]，薛 烽[3]

1. 河海大学 材料科学与工程学院，常州 213200；
2. 中国电建集团 华东勘测设计研究院有限公司，杭州 311122；
3. 东南大学 苏州医疗器械研究院，苏州 215163；
4. 南京工程学院 江苏省先进结构材料与应用技术重点实验室，南京 211167；
5. 宝武镁业科技股份有限公司，南京 211200；
6. 宿迁市河海大学研究院，宿迁 223800

摘 要：为了研究生物可降解锌合金的时效机理并阐明其不稳定组织与性能的关系，采用在 200 ℃退火处理不同时间的工艺对高性能变形 Zn−0.1Mg 合金进行加速时效实验。结果表明，随着退火时间的延长，合金的抗拉强度快速且显著下降。当退火时间达到 1440 min 时，合金的抗拉强度从原始态的 383 MPa 降低到 102 MPa。静态再结晶、晶粒粗化和位错湮灭是合金强度快速下降的主要原因。合金的塑性在退火初期发生波动，随后随着退火时间的延长逐渐降低。塑性的降低与晶粒长大和织构强度的增加有关，而其在退火 30~120 min 的异常增加源于孪晶的形成。此外，由于退火过程中晶粒快速长大、沉淀相和孪晶含量的增加，合金在 Hank's 溶液中的抗腐蚀性能恶化，退火 300 min 后，腐蚀速率从 0.037 mm/a 增加到 0.069 mm/a。

关键词：Zn−0.1Mg 合金；退火；显微组织演变；力学性能；腐蚀行为

(Edited by Wei-ping CHEN)